Research Square

Preprints are preliminary reports that have not undergone peer review.
They should not be considered conclusive, used to inform clinical practice,
or referenced by the media as validated information.

cGAS-STING Pathway Activation Drives PFC Microglial Pyroptosis in Extracellular Vesicle-Related Post-Myocardial Infarction Depression

Rong Zhang

zhangrong@gzucm.edu.cn

Guangzhou University of Chinese Medinicine

Mengxue Chen

Guangzhou University

Fangyuan Chen

Guangzhou University

Ziyi Zeng

Guangzhou University

Ying Yang

Guangzhou University

Qingying Yu

Liuchang Zhou

Yafei Shi

Yuanyuan Cheng

Deng Di

Article

Keywords: Myocardial infarction, Depression, Heart–brain crosstalk, Extracellular vesicles, Mitochondrial DNA, cGAS-STING pathway, Microglial pyroptosis, Prefrontal cortex

Posted Date: October 7th, 2026

DOI: https://doi.org/10.21203/rs.3.rs-10350958/v1

License: This work is licensed under a Creative Commons Attribution 4.0 International License.
Read Full License

Additional Declarations: The authors have declared there is **NO** conflict of interest to disclose

cGAS-STING Pathway Activation Drives PFC Microglial Pyroptosis in Extracellular Vesicle-Related Post-Myocardial Infarction Depression

Mengxue Chen[#1], Fangyuan Chen[#1], Ziyi Zeng[1], Ying Yang[2], Qingying Yu[3], Liuchang Zhou[4], Yafei Shi[2], Yuanyuan Cheng[1], Di Deng*[1], Rong Zhang *[1]

1 State Key Laboratory of Traditional Chinese Medicine Syndrome, Chinese Medicine Guangdong Laboratory, Guangdong Key Laboratory for Translational Cancer Research of Chinese Medicine, Joint International Research Laboratory of Translational Cancer Research of Chinese Medicines, International Institute for Translational Chinese Medicine, Guangzhou University of Chinese Medicine, Guangzhou, 510006, China.

2 School of Fundamental Medical Sciences, Guangzhou University of Chinese Medicine, Guangzhou, 510006, China.

3. The Tenth Clinical Medical College of Guangzhou University of Traditional Chinese Medicine; Zhongshan Hospital of Traditional Chinese Medicine, Zhongshan, 528401, China.

4. Guangdong Provincial Key Laboratory of Clinical Research on Traditional Chinese Medicine Syndrome, The Second Affiliated Hospital of Guangzhou University of Chinese Medicine, Guangzhou, 510120, China.

* Corresponding authors at: 232 Outer Ring East Road, Guangzhou University City, Panyu District, Guangzhou, Guangdong 510006, China.

E-mail addresses: dengdi@gzucm.edu.cn (D Deng), zhangrong@gzucm.edu.cn (R Zhang).

[#]These authors contributed equally.

Abstract

Post-myocardial infarction (MI) depression is a prevalent, severe clinical complication, yet the precise molecular mechanism underlying heart–brain pathological heart–brain crosstalk in this disorder remains poorly elucidated. In this study, we established a mouse MI model with distinct depressive susceptibility phenotypes, including MI-susceptible (MI-sus) and MI-resilient (MI-res) mice, to explore the functional role and regulatory mechanism of plasma extracellular vesicle (EV)-carried mitochondrial DNA (mtDNA) in the pathogenesis of post-MI depression. Our results revealed that MI-sus mice exhibited prominent neuronal injury, synaptic structural disruption and functional dysfunction in the prefrontal cortex (PFC). Mechanistically, plasma EVs derived from MI-sus mice were highly enriched with mtDNA; stereotaxic injection of these EVs into the PFC of healthy naive mice successfully recapitulated depressive-like behaviors and PFC pathological damage. At the molecular level, EV-encapsulated mtDNA triggered microglial innate immune response by activating the cGAS-STING signaling pathway, subsequently inducing microglial pyroptosis and secondary neuronal and synaptic damage in the PFC. Microglia-specific knockdown of cGAS or STING in the PFC markedly attenuated d epressive-like behaviors and reversed PFC pathological lesions in MI mice. Collectively, our findings identify the plasma EV–mtDNA–cGAS-STING–pyroptosis signaling axis as a core molecular mechanism mediating pathological heart–brain crosstalk after myocardial ischemia, offering a novel and actionable therapeutic

target for the clinical prevention and treatment of post-MI depression.

Keywords

Myocardial infarction; Depression; Heart–brain crosstalk; Extracellular vesicles; Mitochondrial DNA; cGAS-STING pathway; Microglial pyroptosis; Prefrontal cortex

Introduction

Despite substantial advances in the clinical diagnosis and intervention of acute myocardial infarction (MI), post-MI depression persists as a common, life-threatening comorbidity[1]. This neuropsychiatric complication not only exacerbates cardiac dysfunction and impairs patients' quality of life but also significantly elevates long-term mortality, constituting a critical unmet clinical challenge[2, 3]. Accumulating clinical and preclinical evidence confirms that aberrant heart–brain crosstalk serves as the core pathological driver of post-MI depression[4].

Peripheral myocardial ischemic injury can induce structural damage and functional dysfunction in corresponding brain regions[5]. The prefrontal cortex (PFC), as the core brain region regulating mood state, cognitive function and emotional homeostasis, is the most vulnerable to such injury[6, 7]. Accumulating evidence has confirmed that neuronal injury, synaptic structural impairment, and dysregulated neuroplasticity in the PFC are closely associated with the onset and severity of depressive phenotypes[8]. Nevertheless, the key molecular mediators that transmit peripheral myocardial ischemic stress signals to the central nervous system and trigger neuropathological damage in the PFC remain largely unclear, which limits the mechanistic interpretation and targeted therapeutic development of post-myocardial infarction depression.

Extracellular vesicles (EVs) are critical intercellular communication vectors capable of transporting diverse bioactive cargoes (proteins, lipids, nucleic acids) across the blood–brain barrier, enabling peripheral injury signals to remotely regulate central immune activation and neural function[9]. Mitochondrial DNA (mtDNA), a typical damage-associated molecular pattern (DAMP) released by damaged mitochondria, is highly enriched in EVs secreted by ischemic-injured cardiomyocytes and can trigger robust innate immune inflammatory responses[10]. Based on these findings, we proposed a core research hypothesis: circulating EVs isolated from depressive-susceptible MI mice carry excessive ischemic injury-derived mtDNA, which acts as a peripheral pathogenic signal targeting the PFC and ultimately induces the occurrence of post-MI depression.

The cGAS-STING pathway is a canonical cytoplasmic DNA-sensing innate immune signaling axis and the primary downstream effector pathway activated by mtDNA stimulation[11]. Once triggered, cGAS-STING signaling initiates the phosphorylation and activation of downstream TBK1/IRF3, promotes NLRP3 inflammasome assembly, and ultimately induces microglial pyroptosis and persistent neuroinflammation[12–14]. As the resident innate immune cells of the CNS, microglia dominate the neuroinflammatory response, mediate synaptic stripping and neuronal injury, and participate in the progression of multiple neuropsychiatric disorders[15, 16]. We further hypothesized that EV-encapsulated mtDNA specifically activates microglial cGAS-STING signaling in the PFC, induces microglial pyroptosis and neuroinflammation, and further causes synaptic dysfunction and depressive-like behaviors after MI.

In the present study, we systematically constructed a mouse MI model with divergent depressive susceptibility phenotypes (MI-sus vs. MI-res) and confirmed that only MI-sus mice developed severe structural and synaptic damage in the PFC. Through EV isolation,

identification and functional verification, interestingly, we validated that mtDNA-enriched plasma EVs from MI-sus mice are sufficient to independently induce depressive-like behaviors and PFC pathological impairment in naive mice. Mechanistically, we clarified that MI-sus-derived EVs specifically activate the cGAS-STING-pyroptosis signaling cascade in PFC microglia, leading to secondary neuronal synaptic dysfunction. Furthermore, microglia-specific knockdown of cGAS or STING effectively reversed MI-induced depressive behaviors and PFC pathological lesions. In summary, this study elucidates a novel heart–brain crosstalk mechanism: plasma EVs shuttle myocardial ischemic mtDNA to the PFC, trigger microglial cGAS-STING-dependent pyroptosis and neuroinflammation, and ultimately mediate post-MI depression. This EV–mtDNA–cGAS-STING–pyroptosis axis provides a promising therapeutic target for post-MI depression.

Methods

Animals and Grouping

Six-to-eight-week-old male C57BL/6J mice were purchased from the Guangdong Medical Laboratory Animal Center (SCXK (Guangdong) 2022-0002). All animal experiments were conducted in the SPF-grade laboratory animal facility of the International Institute for Translational Chinese Medicine, Guangzhou University of Chinese Medicine (SYXK (Guangdong) 2024-0144), and approved by the Institutional Animal Ethics Committee (approval No. 20240307). Mice were housed under standardized conditions (23±2 °C, 60±10% relative humidity, 12 h light/dark cycle) with free access to standard chow and sterile water.

After 1 week of adaptive feeding, mice were randomly assigned to experimental groups. The MI model was established via permanent left anterior descending (LAD) coronary artery ligation; sham-operated mice received identical thoracotomy procedures without arterial ligation[17]. 4 weeks after surgery, MI mice were stratified into MI-sus and MI-res subgroups through behavioral assessments and K-means clustering.

For EV intervention experiments, naive C57BL/6J mice received stereotaxic microinjection of Sham-EV, MI-res-EV or MI-sus-EV into the bilateral PFC, with sample collection and behavioral tests performed 3 days after injection.

For microglia-specific gene knockdown, Cx3Cr1 transgenic mice were stereotaxically injected with AAV-shcGAS, AAV-shSTING or control AAV-shCON, followed by 5 consecutive days of tamoxifen intraperitoneal injection to achieve microglia-specific gene silencing. Two weeks after viral transfection, mice underwent LAD ligation to establish MI models, and behavioral tests were conducted 4 weeks after MI surgery.

Antibody Information

For Western blotting, the following antibodies were used: PSD95 (Servicebio, GB11277, 1:1000), GAP43 (Affinity, DF7766, 1:1000), Synaptophysin (Servicebio, GB11553, 1:1000), cGAS (GeneTex, GTX02874, 1:1000), STING (CST, 50494, 1:1000), p-STING (CST, 72971, 1:1000), p-IRF3 (CST, 29047, 1:1000), p-TBK1 (CST, 5483, 1:1000), NLRP3 (Adipogen, Ag-20b-0014-C100, 1:1000), ASC (Santa Cruz, sc-514414, 1:100), GSDMD (Abcam, ab219800, 1:1000), GSDMD-N (HUABIO, ER1901-37, 1:1000), IL-1β (Bioworld, BS3506, 1:1000), IL-18 (Bioworld, BS6823, 1:1000), Caspase-1 (HUABIO, ET1608-69, 1:50000), P20 (Affinity, AF4005, 1:1000), β-tubulin (Affinity, AF7011, 1:5000), GAPDH (Affinity, AF7021, 1:5000), Vinculin (HUABIO, ET1705-94, 1:5000), TSG101 (ABMART, T55985, 1:5000), CD9 (ABMART, T55337, 1:5000), CD63 (ABMART, M051014, 1:5000), Histone H3 (ABMART, T56587, 1:5000), HRP-conjugated secondary antibodies: Goat anti-rabbit IgG (Signalway Antibody, L3012, 1:5000), Goat anti-Mouse IgG (Signalway Antibody, L3020,

1:5000).

For immunofluorescence: NeuN (Abcam, ab104224, 1:500), GFAP (CST, 3670, 1:400), IBA1 (FUJIFILM Wako, 019-19741, 1:800). cGAS (GeneTex, GTX02874, 1:100), STING (CST, 50494, 1:100), GSDMD (Abcam, ab219800, 1:100), Alexa Fluor® 488 Goat Anti-Rabbit IgG (Abcam, ab150077, 1:500), Alexa Fluor® 594 Goat Anti-Rabbit IgG (Abcam, ab150080, 1:500), Alexa Fluor® 594 Goat Anti-Mouse IgG (Abcam, ab150116, 1:500), Alexa Fluor® 488 Goat Anti-Mouse IgG (Abcam, ab150113, 1:500).

Behavioral Tests

All behavioral tests were initiated 4 weeks after MI modeling. Mice were placed in the behavioral test room for 1 h environmental adaptation before testing. All behavioral performances were recorded by an overhead camera and analyzed by an automatic tracking system with blinded group evaluation[8, 18].

Sucrose Preference Test (SPT): Mice were individually housed for a 72 h adaptive period, followed by 24 h water deprivation. Subsequently, one bottle of 1% sucrose solution and one bottle of sterile water were provided for 24 h. Bottle positions were swapped at 12 h to avoid positional bias. Sucrose preference percentage was calculated as sucrose intake divided by total fluid intake to evaluate anhedonic behaviors.

Open Field Test (OFT): The open field apparatus (50 cm × 50 cm × 40 cm) was divided into central and peripheral zones. Each mouse was placed in the central area for 10 min free exploration. Total movement distance and central zone activity were analyzed to assess locomotor function and anxiety-like behaviors. The apparatus was thoroughly disinfected with 75% ethanol after each test.

Tail Suspension Test (TST): Each mouse was suspended 30 cm above the floor by fixing the distal one-third of the tail with adhesive tape, with no access to climbing support. The total test duration was 6 minutes: the first 2 minutes were for adaptation, and the last 4 minutes were recorded. The immobility time (duration of complete stillness without struggling) was measured as an indicator of behavioral despair.

Forced Swimming Test (FST): Mice were placed in a cylindrical tank filled with water (depth: 30 cm, temperature: 24–26 ℃). The total test duration was 6 minutes: the first 2 minutes were for adaptation, and the last 4 minutes were recorded. Immobility time (floating without active swimming or climbing, only keeping nostrils above water) was measured to assess depression-like despair behavior. After testing, mice were dried and warmed, and the water was replaced before the next test.

Echocardiography

Four weeks after model establishment, mice were anesthetized with pentobarbital sodium (50 mg/kg, i.p.) and fixed in a supine position. After chest depilation and disinfection, M-mode echocardiography was performed using a VINNO6 ultrasound system equipped with a ≥15 MHz high-frequency probe at the left ventricular short-axis papillary muscle level. LVEDD and LVESD were measured, and EF and FS were calculated to evaluate cardiac systolic function. All data were averaged from no less than three independent cardiac cycles.

Histological Staining

Dissected heart and PFC tissues were fixed in 4% paraformaldehyde for 24 h, dehydrated by graded ethanol, cleared with xylene, and embedded in paraffin to prepare 5 μm continuous sections. For H&E staining, sections were deparaffinized, rehydrated, stained with hematoxylin and eosin, differentiated, blued, dehydrated and mounted with neutral balsam for histological morphological observation. For Nissl staining, sections were incubated with 0.1%

toluidine blue solution at 37 °C for 30 min, differentiated with 95% ethanol, fully dehydrated and sealed to observe neuronal morphology and Nissl body distribution.

Transmission electron microscopy (TEM) and Golgi Staining

For synaptic ultrastructural observation, fresh PFC tissues were cut into 1 mm^3 cubes, fixed in pre-cooled electron microscopy fixative at 4 °C for 4 h, post-fixed with 1% osmium tetroxide, fully dehydrated by graded ethanol and pure acetone, infiltrated and embedded with 812 embedding medium, and polymerized at 60 °C. Ultrathin 70 nm sections were stained with 2% uranyl acetate and 2.6% lead citrate for synaptic structure imaging. For EV morphological identification, purified EV suspension was dropped onto copper grids, naturally dried, and negatively stained with 2% uranyl acetate for TEM observation.

Golgi staining was performed using a commercial Golgi staining kit (Servicebio, G1069). Isolated brain tissues were fixed and impregnated in the dark at 4 °C for 7–14 days, dehydrated with 30% sucrose, and prepared into 40 μm frozen sections. After development, cleaning, dehydration and transparency, sections were mounted for observation of neuronal dendritic complexity.

EV Isolation, NTA Detection and mtDNA Quantification

Mouse plasma was collected via EDTA anticoagulation, placed at room temperature for 30 min, and centrifuged at 3000 rpm for 15 min to obtain supernatant plasma. EVs were isolated by gradient centrifugation and ultracentrifugation (120000 g, 70 min, 4 °C), and resuspended in sterile PBS. EV particle size distribution and concentration were detected by nanoparticle tracking analysis. EV mtDNA was extracted using the mtDNA Extractor CT Kit (FUJIFILM Wako, 291-55301). mtDNA quantification was performed via qPCR using SYBR Green qPCR Kit (GOONIE, 500-102) with COXIII-specific primers (Forward: 5'-CCCAGCTACTACCATCATTCAAGT-3'; Reverse: 5'-CAGCCTCATGGTAAACACGTTC-3').

Immunofluorescence Staining

Mice were perfused with PBS and 4% paraformaldehyde. Brain tissues were post-fixed, dehydrated with 20% and 30% sucrose, embedded in OCT, and cut into 40 μm frozen sections. After citrate antigen retrieval, permeabilization and blocking, sections were incubated with primary antibodies overnight at 4 °C, followed by corresponding fluorescent secondary antibodies. Finally, sections were mounted with anti-fade medium and observed under a fluorescence microscope.

PFC Stereotaxic Injection

Mice were anesthetized with isoflurane and fixed on a stereotaxic instrument. The adeno-associated viruses used in this study were rAAV-SFFV-DIO-mCherry-5'-miR-30a-shRNA(scramble)-3'-miR-30a-WPREs、rAAV-SFFV-DIO-mCherry-5'-miR-30a-shRNA (Cgas)-3'-miR-30a-WPREs and rAAV-SFFV-DIO-mCherry-5'-miR-30a-shRNA (sting)-3'-miR-30a-WPREs, all purchased from Wuhan Shumi Brain Science Technology Co., Ltd. PFC injection coordinates were set as AP +1.94 mm, ML ±0.2 mm, DV −2.4 mm. For EV injection, 40 μg EVs were bilaterally injected at a rate of 0.2 μL/min, with the needle retained for 4 min after injection to ensure full diffusion. For AAV injection, a total volume of 0.5 μL virus was injected into each hemisphere with identical injection parameters. Postoperative mice were placed on a constant-temperature heating platform for recovery before rearing。

Cell Culture and Intervention

BV2 microglial cells (CL-0493) and HT-22 neuronal cells (CL-0697) were purchased from Procell Life Science & Technology Co., Ltd., and cultured at 37 °C with 5% CO_2. For

siRNA transfection, BV2 cells were transfected with si-Cgas (RX25061906456, Hippobio) and si-Sting (RX25061906457, Hippobio) using Lipofectamine 2000 (Thermo Fisher, 11668019) for 48 h. EVs were labeled with FluoExo® Exosome Tracing Kit (Engreen Biosystem, FE-01-02) for cell internalization detection. BV2 cells were treated with 32 μg/mL Sham-EV, MI-res-EV or MI-sus-EV for 24 h. The conditioned medium of EV-activated BV2 cells was collected to treat HT-22 neurons for synaptic function evaluation.

Statistical Analysis

Data were analyzed using SPSS 21.0 and GraphPad Prism 9.2.0, presented as mean ± SD. Shapiro–Wilk test was used for normality assessment. Normally distributed data with homogeneous variance were analyzed by one-way ANOVA; data with heterogeneous variance were analyzed by Brown-Forsythe and Welch ANOVA, followed by Bonferroni multiple comparison test. Non-normal data were analyzed by Kruskal–Wallis H test. $P < 0.05$ was considered statistically significant.

Results

MI induces depressive-like behaviors and PFC tissue damage in mice

To explore the behavioral and pathological changes of depression after MI, a mouse MI model was established via LAD artery ligation in male C57BL/6J mice (Fig. 1a). H&E staining showed disordered myocardial tissue structure, and echocardiographic detection confirmed significantly reduced ejection fraction (EF%) and fractional shortening (FS%) in MI groups (Fig. S1a–d), verifying the successful construction of a stable and reliable mouse MI model.

28 days after surgery, depressive-like behaviors of mice were evaluated via behavioral tests, TEMand K-means clustering analysis was applied to stratify MI mice into two subgroups with distinct phenotypes: MI-resilient (MI-res) and MI-susceptible (MI-sus)[19, 20]. Behavioral results showed that MI-sus mice exhibited typical depressive-like phenotypes, including significant anhedonia in the sucrose preference test and prolonged immobility time in the tail suspension test (TST) and forced swim test (FST) (Fig. 1b, e, f). No significant difference in spontaneous locomotor activity was observed among groups in the open field test (Fig. 1c, d), indicating that the behavioral differences were independent of motor function and truly reflected depressive susceptibility.

Histopathological staining revealed obvious structural damage in the PFC of MI-sus mice, characterized by disordered neuronal arrangement, nuclear pyknosis and decreased Nissl body number (Fig. 1g, h). TEM further demonstrated disrupted synaptic ultrastructure (Fig. 1i–m). Golgi staining showed reduced dendritic complexity and arborization of PFC neurons (Fig. 1n–t). Consistent with morphological changes, Western blot results confirmed the significant downregulation of synaptic functional proteins (PSD95, GAP43, SYN) in the PFC of MI-sus mice (Fig. 1u–x). Notably, MI-res mice only presented mild PFC pathological changes without obvious depressive-like behaviors, indicating that the severity of PFC structural and synaptic damage is positively correlated with individual depressive susceptibility after MI, and MI-res mice may possess endogenous compensatory protective mechanisms against post-MI emotional dysfunction.

EVs from MI-sus mice trigger depressive-like phenotypes and synaptic impairment in the PFC

EVs are key intercellular communication carriers that cross the blood–brain barrier to transmit peripheral injury signals and regulate central neural function, which is considered a

critical medium for peripheral-central crosstalk[21]. Combined with the specific PFC damage in MI-sus mice, we further explored whether plasma EVs mediate the occurrence of post-MI depression.

Plasma EVs were isolated from Sham, MI-res and MI-sus mice, and EV morphology, particle size distribution and specific marker expression were verified by TEM, nanoparticle tracking analysis (NTA) and Western blotting (Fig. 2b–d), confirming the high purity and quality of isolated EVs for subsequent experiments[22]. Quantitative detection showed that mtDNA content was significantly elevated in EVs derived from MI-sus mice (Fig. 2e), suggesting that myocardial ischemic injury induces mitochondrial damage and releases abundant mtDNA into circulating EVs, which may serve as a key pathogenic cargo mediating peripheral-to-central signal transmission.

Stereotaxic injection of MI-sus-derived EVs into the PFC of naive healthy mice (Fig. 2a) successfully induced typical depressive-like behaviors, including reduced sucrose preference and increased immobility in TST and FST, with no alteration in locomotor activity (Fig. 2f–j). In contrast, EVs from MI-res mice failed to induce obvious depressive phenotypes, indicating that the neuro-pathogenic effect of circulating EVs is specifically dependent on the depressive susceptibility of MI mice.

Consistent with behavioral changes, MI-sus-EV treatment caused severe neuronal damage in the mouse PFC, including disordered cell arrangement, nuclear pyknosis and reduced Nissl bodies. Meanwhile, the expression levels of synaptic proteins PSD95, GAP43 and SYN were significantly downregulated (Fig. 2k–p). The above neuronal and synaptic impairments were negligible in the MI-res-EV intervention group. Collectively, these results demonstrate that mtDNA-enriched EVs from MI-sus mice independently mediate PFC structural destruction and synaptic dysfunction, thereby driving the development of post-MI depressive-like behaviors.

Activation of cGAS-STING and pyroptosis in PFC and EV-mediated BV2 cells in post-MI depression

Given that mtDNA is a specific agonist of the microglial cGAS-STING innate immune pathway, we further explored whether EV-carried mtDNA induces PFC damage by activating cGAS-STING signaling and downstream pyroptosis in post-MI depression.

Western blot analysis of mouse PFC tissues showed that the key proteins of the cGAS-STING signaling pathway (cGAS, p-STING, p-TBK1, p-IRF3) and pyroptosis-related proteins (NLRP3, ASC, Caspase 1, P20, GSDMD-N, IL-1β, IL-18) were significantly upregulated in the MI-sus group, while no obvious activation was observed in the MI-res group (Fig. 3a–c). These results indicate that the cGAS-STING-pyroptosis signaling cascade is specifically hyperactivated in the PFC of depression-susceptible MI mice.

In vivo EV intervention experiments further verified that stereotaxic injection of MI-sus-EVs into naive mice was sufficient to activate cGAS-STING signaling and upregulate pyroptosis-related protein expression in the PFC (Fig. 3d–f), confirming that MI-sus-EVs are the key trigger for central cGAS-STING pathway activation.

Immunofluorescence co-localization staining showed that cGAS, STING and GSDMD were predominantly expressed in IBA-1-positive microglia in the mouse PFC (Fig. 4a–f), confirming that microglia are the primary cellular substrate for cGAS-STING-dependent pyroptosis in post-MI brain injury.

In vitro, consistent with in vivo findings, MI-sus-EV intervention significantly activated the cGAS-STING pathway and pyroptosis in BV2 microglial cells (Fig. S2a–d). Moreover,

the conditioned medium of MI-sus-EV-treated BV2 cells markedly reduced the expression of synaptic proteins PSD95 and SYN in HT22 hippocampal neurons (Fig. S2e–g). These in vitro and in vivo results jointly demonstrate that EV-induced microglial cGAS-STING activation and pyroptosis trigger secondary neuronal synaptic damage, forming a pathogenic microglia-neuron crosstalk loop in post-MI depression.

cGAS-STING deficiency ameliorates post-MI depression and PFC synaptic injury

To further validate the indispensable role of microglial cGAS-STING signaling in post-MI depression, we constructed microglia-specific cGAS/STING knockdown mouse models via stereotaxic injection of AAV-shcGAS, AAV-shSTING or control AAV into the PFC of Cx3Cr1 mice, with tamoxifen-induced targeted gene knockdown (Fig. 5a). Fluorescence imaging confirmed accurate viral targeting in the PFC (Fig. S3e). Cardiac H&E staining and echocardiography verified consistent myocardial injury and cardiac dysfunction among all MI groups, with no significant differences between virus intervention subgroups (Fig. S3a–d), excluding the confounding effect of cardiac function changes on behavioral and central pathological results.

Behavioral tests showed that microglial cGAS or STING knockdown significantly alleviated MI-induced anhedonia and despair-like behaviors in mice (Fig. 5b–f). Histopathological staining showed that cGAS/STING silencing effectively improved MI-induced PFC neuronal disorder and nuclear condensation, restored Nissl body abundance (Fig. 5g, h). TEM and Golgi staining further confirmed that cGAS-STING inhibition rescued synaptic ultrastructural damage and reversed the reduction of neuronal dendritic complexity in the PFC of MI mice (Fig. 5i–t).

Molecular detection results showed that microglial cGAS/STING knockdown significantly reversed the downregulation of synaptic plasticity proteins (PSD95, GAP43, SYN) and inhibited the excessive activation of cGAS-STING signaling and downstream pyroptosis in the PFC of MI mice (Fig. 6a–g). In vitro experiments also verified that cGAS/STING gene silencing blocked MI-sus-EV-induced cGAS-STING activation and pyroptosis in BV2 microglia (Fig. 6h–j). Collectively, these loss-of-function experiments fully demonstrate that microglial cGAS-STING signaling is an essential molecular switch for EV-mediated PFC pyroptotic injury and post-MI depressive-like behaviors. The detailed regulatory mechanism is summarized in the schematic diagram (Fig. 6k).

Discussion

Although growing research has identified aberrant heart–brain crosstalk as a pivotal pathological driver of post-MI depression[23], mounting evidence has validated that dysfunction of prefrontal cortical synaptic plasticity is closely involved in the onset and exacerbation of depression[8, 24, 25]. Structural synaptic loss and impaired synaptic remodeling within the PFC are well-established core pathological features mediating emotional disturbance and depressive-like behaviors, the intrinsic mechanisms underlying the variable susceptibility to depressive symptoms following MI remain poorly elucidated, restricting the in-depth understanding and targeted intervention of this common MI comorbidity. In the present study, we successfully constructed a mouse MI model with distinct individual susceptibility to post-MI depression and comparatively analyzed the pathological alterations in the PFC between MI-sus and MI-res mice. Consistent with our hypothesis, the severity of neuronal injury and synaptic structural impairment in the PFC was verified to be a key determinant of individual differences in post-MI depressive vulnerability.

These findings clarify the central pathological difference accounting for the heterogeneous onset of post-MI depression, offering novel neuropathological evidence to elaborate the heart–brain regulatory mechanism of post-MI emotional dysfunction.

Different from previous studies focusing on central neuroinflammation after MI[17], emerging researches have demonstrated that EVs participate in the pathological processes of myocardial injury and depression[26, 27], and serve as important messengers for peripheral-central signal transmission. This study further innovatively identified plasma EVs as the key peripheral mediator linking myocardial ischemic insult to prefrontal cortex damage. Multiple lines of evidence in our study support this conclusion: EVs isolated from MI-sus mice with depressive phenotypes are highly enriched with mtDNA, a typical injury-related molecular pattern; exogenous supplementation of MI-sus-EVs alone can recapitulate post-MI depressive behaviors and PFC pathological damage in healthy mice, while EVs from resilient mice have less neuro-pathogenic effect. Myocardial ischemia induces severe mitochondrial damage in cardiomyocytes, leading to the release of a large amount of mtDNA into the peripheral circulation[10]. This study verified that ischemic mtDNA is wrapped and protected by EVs. Given that EVs have been proven in prior studies to penetrate the blood–brain barrier and target the PFC[28, 29], our results clarify the specific molecular pattern of peripheral ischemic signals invading the central nervous system and address the research gap in the upstream mechanism of heart–brain crosstalk in post-MI depression. Notably, our work shifts the focus from inflammatory mediators to circulating EVs as the primary upstream carrier, establishing a direct and specific molecular link between cardiac ischemia and PFC injury.

The cGAS-STING pathway is a classic innate immune sensor for cytoplasmic foreign DNA and damage-derived self-DNA[30]. In this study, we verified that mtDNA carried by MI-sus-EVs specifically activates the cGAS-STING signaling cascade in PFC microglia, rather than neurons or astrocytes. Activated cGAS-STING signaling further promotes NLRP3 inflammasome assembly, triggers microglial pyroptosis and massive release of pro-inflammatory cytokines, ultimately causing synaptic destruction and neuronal dysfunction. Numerous prior studies have confirmed that cGAS-STING pathway activation can initiate NLRP3 inflammasome response and induce cellular pyroptosis[14, 31, 32], which is also fully verified in our current study. In vitro co-culture experiments verified that pyroptotic microglia release inflammatory mediators and impair neuronal synaptic integrity. Previous studies have demonstrated that microglia regulate neuronal synaptic plasticity via synaptic pruning[33–35]. Notably, this study merely confirmed the paracrine damage effect induced by inflammatory factors, without exploring direct contact interaction between microglia and neurons. Collectively, these results establish a complete pathological cascade: peripheral EV-carried mtDNA triggers cGAS-STING signaling and pyroptosis in microglia, further leading to neuronal synaptic defects and ultimately facilitating the development of depressive-like behaviors. This finding clarifies the cell-specific regulatory mechanism of cGAS-STING signaling in post-MI depression and enriches the mechanistic understanding of microglia-mediated neuroinflammatory psychiatric disorders.

More importantly, microglia-specific cGAS or STING knockdown in vivo can significantly inhibit PFC pyroptosis and neuroinflammation, restore synaptic structural integrity and neuronal function, and fundamentally improve MI-induced depressive-like behaviors, without affecting the degree of myocardial injury. These functional verification results confirm that microglial cGAS-STING signaling is a necessary and sufficient condition for post-MI depression, providing precise and targeted therapeutic targets for the clinical

intervention of post-MI depression and avoiding the non-specific side effects of systemic immune pathway intervention.

This study has important translational clinical implications. First, mtDNA has already been recognized as a promising circulating biomarker for myocardial infarction and depression, with established value in disease stratification and prognostic prediction[36–38]. On this basis, plasma EV-encapsulated mtDNA can serve as a novel non-invasive biomarker for early screening of populations susceptible to post-MI depression, facilitating early risk prediction and targeted intervention in high-risk patients. Second, the newly identified EV–mtDNA–cGAS-STING–pyroptosis axis systematically explains the molecular mechanism of heart–brain crosstalk in post-MI depression, providing a theoretical framework for subsequent related basic and clinical research. Third, targeted inhibition of microglial cGAS-STING signaling or pyroptosis is expected to become a new therapeutic strategy for preventing and treating post-MI depression.

This study also has certain limitations that need to be improved in future research. First, this study only focused on plasma EVs as the core regulatory vector; other circulating cytokines[39, 40] and EV subtypes may also participate in the progression of post-MI depression and mediate peripheral-central neural transmission between the heart and brain[41, 42], which warrants further exploration. Second, besides mtDNA, MI-sus-EVs contain multiple bioactive cargoes, and whether these molecules synergistically regulate central neuroinflammation as well as heart-brain neural communication remains to be verified. Third, the endogenous protective compensatory mechanism of MI-res mice against post-MI depression was not deeply explored in this study, which is worthy of further excavation to develop new protective therapeutic targets.

In conclusion, this study elucidates a novel heart–brain crosstalk mechanism in post-MI depression: plasma EVs transport myocardial ischemia-derived mtDNA to the PFC, specifically activate microglial cGAS-STING signaling pathway, induce microglial pyroptosis and persistent neuroinflammation, and ultimately lead to neuronal synaptic damage and depressive-like behaviors. This study establishes a new pathogenic signaling axis for post-MI depression and provides a reliable theoretical basis for the development of targeted therapeutic strategies.

References

1. Ruan W, Li T, Bang IH, Lee J, Deng W, Ma X, et al. BMAL1-HIF2A heterodimer modulates circadian variations of myocardial injury. Nature. 2025;641:1017–1028.
2. Michelsen HÖ, Lidin M, Bäck M, Duncan TS, Ekman B, Hagström E, et al. The effect of audit and feedback and implementation support on guideline adherence and patient outcomes in cardiac rehabilitation: a study protocol for an open-label cluster-randomized effectiveness-implementation hybrid trial. Implement Sci. 2024;19:35.
3. Henderson C, Gillard C, Wheeler JB, Maestri T, Smith C, Olet S. The Impact of Post-Myocardial Infarction (MI) Depression on Cardiovascular-Related Hospitalizations. Curr Probl Cardiol. 2023;49:102070.
4. Valenza G, Matić Z, Catrambone V. The brain-heart axis: integrative cooperation of neural, mechanical and biochemical pathways. Nat Rev Cardiol. 2025;22:537–550.
5. Chen E, Zhu X, Chang H, Li Q, Zhao Z, Zhang C, et al. Targeting cardiomyocyte-derived extracellular vesicle miR-574-5p protects against cognitive impairment

induced by ischemia-reperfusion. BMC Med. 2026;24:298.
6. Moazzami K, Wittbrodt MT, Lima BB, Nye JA, Mehta PK, Pearce BD, et al. Higher Activation of the Rostromedial Prefrontal Cortex During Mental Stress Predicts Major Cardiovascular Disease Events in Individuals With Coronary Artery Disease. Circulation. 2020;142:455–465.
7. Zhang Y, Wang X, Li Y, Liu R, Pan J, Tang X, et al. Human umbilical cord mesenchymal stem cells ameliorate depression by regulating Jmjd3 and microglia polarization in myocardial infarction mice. Psychopharmacology (Berl). 2021;238:2973–2984.
8. Xie Z, Chen M, Yi W, Wang S, Deng D, An L, et al. Jieyu Wuwei Sinisan formula alleviates depression-like behaviors in CUMS mice by regulating synaptic plasticity through PLD2 pathway. J Ethnopharmacol. 2026;356:120841.
9. Liao K, Yu J, Mohammadigoldar Z, Li J, Liu W, Li L, et al. Heart-Brain Crosstalk in Myocardial Infarction: Role of Heart Extracellular Vesicles in Neuroinflammation. Circ Res. 2025;136:1513–1515.
10. Zhang C, Hao H, Wang Y, Mu N, Jiang W, Zhang Z, et al. Intercellular mitochondrial component transfer triggers ischemic cardiac fibrosis. Sci Bull (Beijing). 2023;68:1784–1799.
11. Zhang B, Xu P, Ablasser A. Regulation of the cGAS-STING Pathway. Annu Rev Immunol. 2025;43:667–692.
12. Zhang X, Bai X-C, Chen ZJ. Structures and Mechanisms in the cGAS-STING Innate Immunity Pathway. Immunity. 2020;53:43–53.
13. Rouhi L, Gurha P, Marian AJ. The CGAS-STING1 Pathway as a Mediator of Innate Immune Response in Cardiovascular Disease. JACC Asia. 2025;5:516–527.
14. Ding R, Li H, Liu Y, Ou W, Zhang X, Chai H, et al. Activating cGAS-STING axis contributes to neuroinflammation in CVST mouse model and induces inflammasome activation and microglia pyroptosis. J Neuroinflammation. 2022;19:137.
15. Feng X, Zhao Y, Yang T, Song M, Wang C, Yao Y, et al. Glucocorticoid-Driven NLRP3 Inflammasome Activation in Hippocampal Microglia Mediates Chronic Stress-Induced Depressive-Like Behaviors. Front Mol Neurosci. 2019;12:210.
16. Silva-Llanes I, Smith LA, Abdelkader-Guillén A, Jiménez-Villegas J, Sarrió D, Moreno-Bueno G, et al. GASDERMIN D-mediated pyroptosis as a therapeutic target in TAU-dependent frontotemporal dementia mouse model. J Biomed Sci. 2026;33:6.
17. Yang Y, Huang T, Zhang H, Li X, Shi S, Tian X, et al. Formononetin improves cardiac function and depressive behaviours in myocardial infarction with depression by targeting GSK-3β to regulate macrophage/microglial polarization. Phytomedicine. 2023;109:154602.
18. Wang Y, Liu Z, Wu J, Ye L, Huang C, Xuan Y, et al. Si-Ni-San alleviates depressive-like behaviors in adolescent male mice by restoring DRN-NAc serotonergic circuit function and 5-HT4R-dependent synaptic plasticity. Phytomedicine. 2026;155:158088.
19. Wang Q, Wang X, Lv Y, Yang C, Zhou C, Wang L. Changes in Rats' Gut Microbiota Composition Caused by Induced Chronic Myocardial Infarction Lead to Depression-Like Behavior. Front Microbiol. 2021;12:641084.

20. Loizeau V, Durieux L, Mendoza J, Wiborg O, Barbelivien A, Lecourtier L. Behavioural characteristics and sex differences of a treatment-resistant depression model: Chronic mild stress in the Wistar-Kyoto rat. Behav Brain Res. 2024;457:114712.
21. Ohayon-Steckel L, Zhang X, Haque S, Uddin MA, Dasari A, Kurian DG, et al. miR-499 in Platelet-Derived Extracellular Vesicles Augments Inflammatory Cell Generation and Cardiac Remodeling After Myocardial Infarction. Circulation. 2026;153:243–259.
22. Davidson SM, Boulanger CM, Aikawa E, Badimon L, Barile L, Binder CJ, et al. Methods for the identification and characterization of extracellular vesicles in cardiovascular studies: from exosomes to microvesicles. Cardiovasc Res. 2023;119:45–63.
23. Yadav S, Ninh VK, Lovelace JW, Ma J, Pham A, Salamon RJ, et al. A triple-node heart-brain neuroimmune loop underlying myocardial infarction. Cell. 2026;189:800-817.e20.
24. Brown KA, Ajibola MI, Medeiros GC, Gould TD. Synaptic priming: A framework for pharmacotherapy in depression. Neuron. 2025;113:3722–3740.
25. Horchar MJ, Wohleb ES. Glucocorticoid receptor antagonism prevents microglia-mediated neuronal remodeling and behavioral despair following chronic unpredictable stress. Brain Behav Immun. 2019;81:329–340.
26. Wang F, Yang J, Wang G. Exosomes in depression: mechanistic insights, diagnostic potential, and therapeutic opportunities. Mol Psychiatry. 2026. 28 April 2026. https://doi.org/10.1038/s41380-026-03622-3.
27. Omoto ACM, Vechetti I, do Carmo JM, Wang Z, Mouton AJ, Young JC, et al. Leptin Activates Brain-BAT-Heart Crosstalk to Promote Cardiac Protection. Circ Res. 2026;138:e326878.
28. Yu S, Cheng Q, Yu Q, Cui Z, Chen H, Wu S, et al. Systemic LINE-1 RNA in Plasma Extracellular Vesicles Drives Neuroinflammation and Cognitive Dysfunction via cGAS-STING Pathway in Aging. Aging Cell. 2026;25:e70350.
29. Kaur M, Fusco S, Van den Broek B, Aseervatham J, Rostami A, Iacovitti L, et al. Most recent advances and applications of extracellular vesicles in tackling neurological challenges. Med Res Rev. 2024;44:1923–1966.
30. Cai Y, Zhou T, Sun J, Cai X, Shi W, Chen J, et al. DHCR24 Deficiency Drives Age-Related Meibomian Gland Dysfunction by Regulating Lipid Metabolic Imbalance and Cytosolic mtDNA-Induced cGAS-STING Activation. Int J Biol Sci. 2026;22:3886–3908.
31. Li Q, Feng L, Tian Y, Guo E, Li Y, Niu J, et al. Melatonin alleviates neuroinflammation in ischemic stroke by regulating cyclic GMP-AMP synthase- mediated microglial pyroptosis signaling. Neural Regen Res. 2026;21:2380–2388.
32. Dai Y, Chen Z, Zhu W, Wang S, Ren X, Yang Y, et al. Trihexyl phosphate exposure disrupts mitophagy and activates mtDNA-cGAS-STING signaling to drive pyroptosis and steroidogenic impairment in Leydig cells. J Hazard Mater. 2026;507:141827.
33. Paolicelli RC, Bolasco G, Pagani F, Maggi L, Scianni M, Panzanelli P, et al. Synaptic pruning by microglia is necessary for normal brain development. Science. 2011;333:1456–1458.
34. Tang Y, Huang Y, Pan J, Li C, Yang J, Tan X, et al. IL-15 receptor alpha deficiency triggers depressive-like behaviors via enhanced microglial synapse pruning. Mol

Psychiatry. 2026. 22 April 2026. https://doi.org/10.1038/s41380-026-03593-5.
35. Chen X, Zhang K, Li Y, Wang C, Lou H, Yu S. Stress induces behavioral disorders by promoting microglial phagocytosis via decreasing neuronal Dkk3. Mol Psychiatry. 2025;30:5731–5748.
36. Cosentino N, Campodonico J, Moltrasio M, Lucci C, Milazzo V, Rubino M, et al. Mitochondrial Biomarkers in Patients with ST-Elevation Myocardial Infarction and Their Potential Prognostic Implications: A Prospective Observational Study. J Clin Med. 2021;10:275.
37. Koller A, Fazzini F, Lamina C, Rantner B, Kollerits B, Stadler M, et al. Mitochondrial DNA copy number is associated with all-cause mortality and cardiovascular events in patients with peripheral arterial disease. J Intern Med. 2020;287:569–579.
38. Ye J, Duan C, Han J, Chen J, Sun N, Li Y, et al. Peripheral mitochondrial DNA as a neuroinflammatory biomarker for major depressive disorder. Neural Regen Res. 2025;20:1541–1554.
39. Zhang L, Liu M, Chen H, Li Y, Rao P. Antidepressant in treating myocardial infarction complicated with depression via 5-HT/inflammation from heart to brain. J Affect Disord. 2025;391:120048.
40. Patel P, Yang F, Iacobas DA, Xi L. Mental disorders after myocardial infarction: potential mediator role for chemokines in heart-brain interaction? J Geriatr Cardiol. 2024;21:913–926.
41. Xu X, Qiao J, Wang Y, Liu Z, Liu Z, Tan W, et al. PENG-based self-powered transcutaneous auricular vagus nerve stimulation attenuated myocardial infarction-induced heart-brain remodeling via ameliorating the neuroinflammatory response in central amygdala. Int Immunopharmacol. 2025;162:115085.
42. Huynh P, Hoffmann JD, Gerhardt T, Kiss MG, Zuraikat FM, Cohen O, et al. Myocardial infarction augments sleep to limit cardiac inflammation and damage. Nature. 2024;635:168–177.

Author Contributions

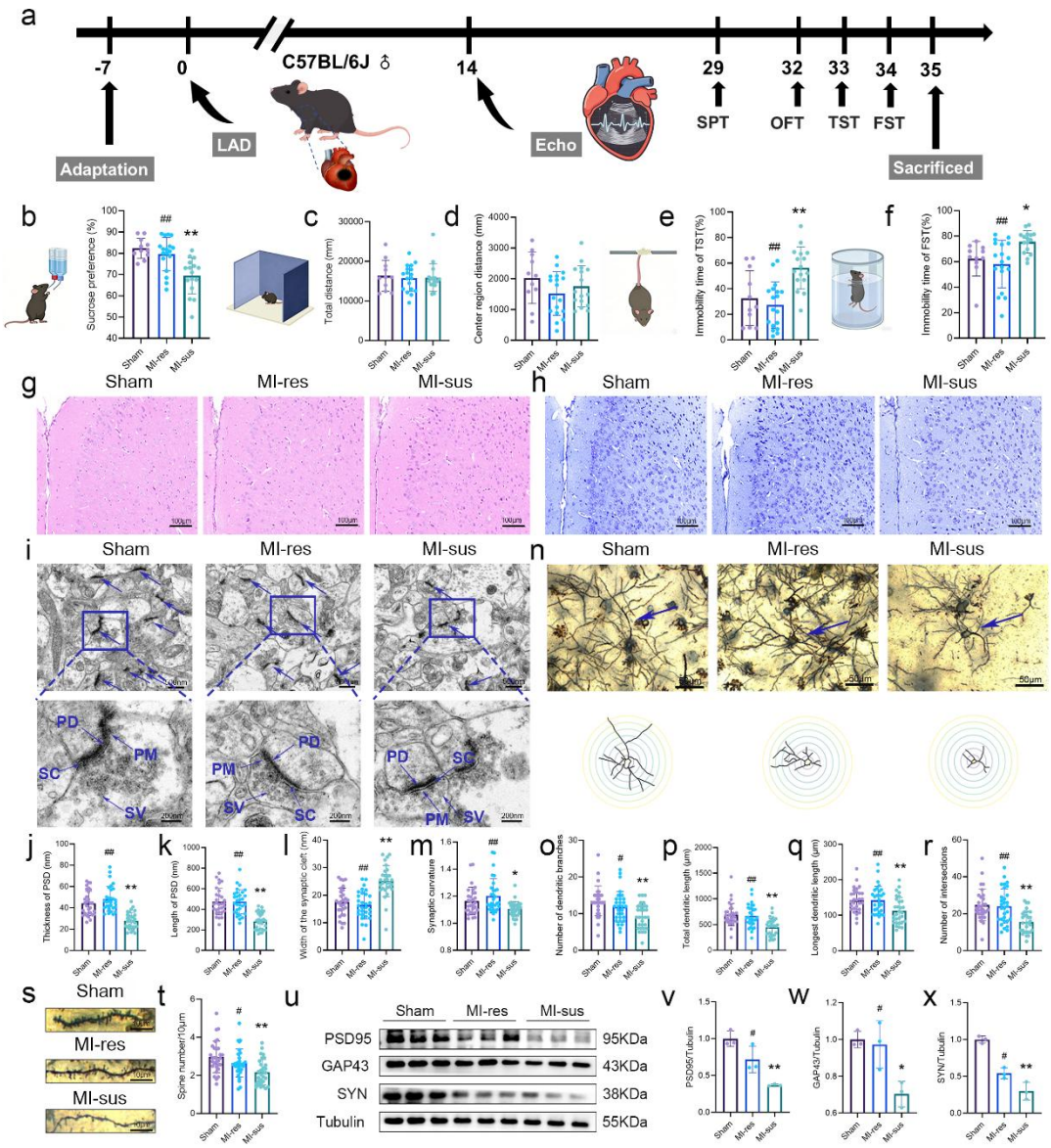
Conceptualization: R.Z., D.D., and M.C. conceived and designed the study. Experimentation: R.Z., D.D., and M.C. designed the experiments; M.C., F.C., Z.Z., Y.Y., and Q.Y. executed the experiments. Data Analysis: M.C., F.C., Z.Z, Y.Y., and Q.Y. performed data analysis; M.C. and F.C. performed the bioinformatics analysis. Writing and Revision: M.C., F.C., Z.Z., Y.Y., and Q.Y. drafted the manuscript; L.Z., Y.S., Y.C., D.D., and R.Z. revised the manuscript. Funding acquisition: R.Z., D.D., L.Z., and Y.S. acquired funding support.

Funding

We would like to thank everyone who took part in this study. This research was supported by the National Natural Science Foundation of China (U24A20791, 82274226, 82405254, 82274443), Science and Technology Key Projects in Guangzhou (2023B03J1238), Sanming Project of Medicine in Shenzhen (SZZYSM202206005), Science and Technology Planning Project of Guangdong Province (2025A1515011906), Guangdong University Key Areas Special Project(2024ZDZX2039), and Chinese Medicine Guangdong Laboratory (HQL2024PZ030).

Competing Interests

The authors declare no conflict of interest.


a
-7
0
14
29
32
33
34
35
C57BL/6J ♂
Adaptation
LAD
Echo
SPT
OFT
TST
FST
Sacrificed
b
Sucrose preference (%)
c
Total distance (mm)
d
Center region distance (mm)
e
Immobility time of TST(%)
f
Immobility time of FST(%)
Sham
MI-res
MI-sus
g
h
i
n
PD
PM
SC
SV
j
Thickness of PSD (nm)
k
Length of PSD (nm)
l
Width of the synaptic cleft (nm)
m
Synaptic curvature
o
Number of dendritic branches
p
Total dendritic length (μm)
q
Longest dendritic length (μm)
r
Number of intersections
s
t
Spine number/10μm
u
PSD95
GAP43
SYN
Tubulin
95KDa
43KDa
38KDa
55KDa
v
PSD95/Tubulin
w
GAP43/Tubulin
x
SYN/Tubulin

590
591

Fig 1 MI induces depressive-like behaviors and PFC tissue damage in mice

(a) Schematic diagram of the experimental timeline.

(b–f) Quantitative analysis of sucrose preference (b), total movement distance (c), central region distance (d), immobility time in TST (e)and immobility time in FST (f) among groups, n = 11 (Sham), 18 (MI-res), 16 (MI-sus), One-way ANOVA (b, d, e) and Kruskal-Wallis test (c, f), *p<0.05, **p<0.01, vs Sham, $^{\#}p$<0.05, $^{\#\#}p$<0.01, vs MI-sus.

(g) Representative H&E staining of the PFC in the three groups. Scale bar, 100 μm.

(h) Representative Nissl staining of the PFC in the three groups. Scale bar, 100 μm.

(i) Representative TEM micrographs of synapses in the PFC, with presynaptic membrane (PM), postsynaptic density (PD), synaptic cleft (SC), and synaptic vesicles (SV) labeled. Scale bar, 500 nm and 200 nm.

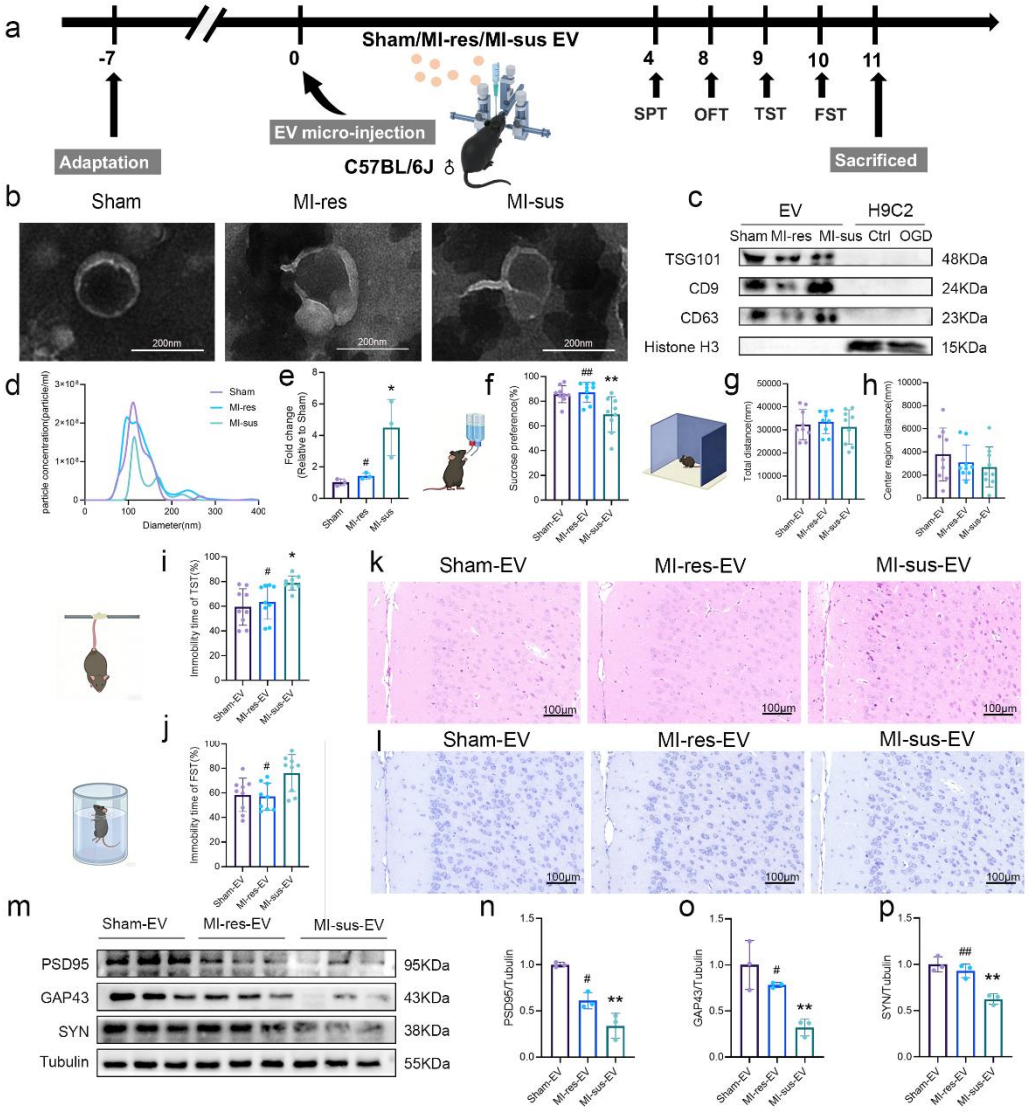
(j–m) Quantification of PSD thickness (j), PSD length (k), width of the synaptic cleft (l) and synaptic curvature (m) in the PFC, n=3 mice per group, with 10 synapses analyzed per mouse, One-way ANOVA (l) and Kruskal-Wallis test (j, k, m), *p<0.05, **p<0.01, vs Sham, $^{\#}p$<0.05, $^{\#\#}p$<0.01, vs MI-sus,(n) Representative Golgi staining of pyramidal neurons in the PFC and corresponding Sholl analysis diagrams showing dendritic complexity. Arrows point to representative pyramidal neurons, scale bar, 50 μm.

(o–r) Quantification of the number of dendritic branches (o), total dendritic length (p), longest dendritic length (q), and number of intersections (r) by Sholl analysis, n=3 mice per group, with 10 neurons analyzed per mouse, One-way ANOVA (q) and Kruskal-Wallis test (o, p, r), *p<0.05, **p<0.01, vs Sham, $^{\#}p$<0.05, $^{\#\#}p$<0.01, vs MI-sus.

(s) Representative images of dendritic spines in the PFC. Scale bar, 10 μm.

(t) Quantification of spine density in the three groups, n=3 mice per group, with 10 dendritic segments analyzed per mouse, One-way ANOVA **p<0.01, vs Sham, $^{\#}p$<0.05, vs MI-sus.

(u–x) Western blot analysis (u) and quantification of synaptic proteins PSD95 (v), GAP43 (w), and SYN (x) in the PFC, n=3 mice per group. One-way ANOVA, *p<0.05, **p<0.01, vs Sham, $^{\#}p$<0.05, vs MI-sus, Data are expressed as mean ± SD.


a
Sham/MI-res/MI-sus EV
-7
0
4
8
9
10
11
SPT
OFT
TST
FST
Adaptation
EV micro-injection
C57BL/6J ♂
Sacrificed
b
Sham
MI-res
MI-sus
200nm
c
EV
H9C2
Sham MI-res MI-sus Ctrl OGD
TSG101
CD9
CD63
Histone H3
48KDa
24KDa
23KDa
15KDa
d
particle concentration(particle/ml)
Diameter(nm)
Sham
MI-res
MI-sus
e
Fold change (Relative to Sham)
f
Sucrose preference(%)
g
Total distance(mm)
h
Center region distance(mm)
i
Immobility time of TST(%)
j
Immobility time of FST(%)
Sham-EV
MI-res-EV
MI-sus-EV
k
l
100μm
m
PSD95
GAP43
SYN
Tubulin
95KDa
43KDa
38KDa
55KDa
n
PSD95/Tubulin
o
GAP43/Tubulin
p
SYN/Tubulin

622
623

Fig 2 EVs from MI-sus mice trigger depressive-like phenotypes and synaptic impairment in the PFC

(a) Schematic diagram of the experimental timeline.

(b) Representative TEM images of EV isolated from Sham, MI-res, and MI-sus mice. Scale bar, 200 nm.

(c) Western blot analysis of EV markers (TSG101, CD9, CD63) and the negative control (Histone H3) in isolated EVs. H9C2 whole-cell lysate was used as the control.

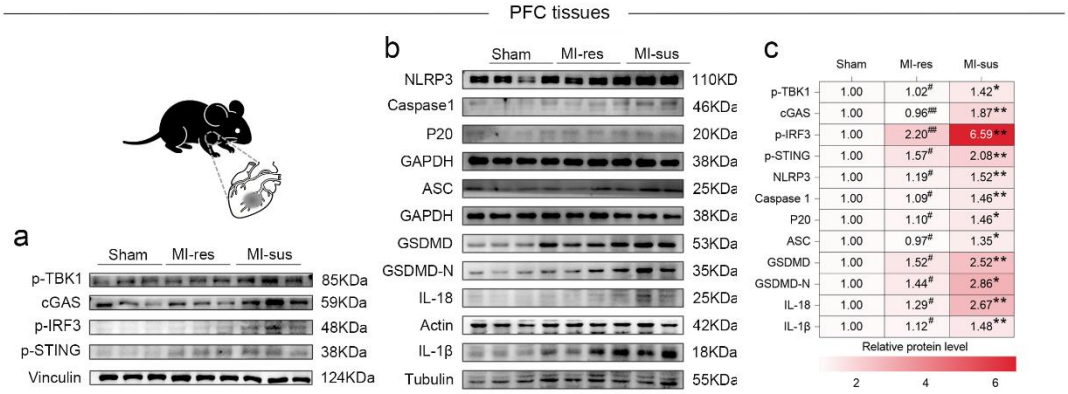
(d) NTA showing the particle size distribution of EVs from Sham, MI-res, and MI-sus mice. (e) Quantification of EV particle concentration (fold change relative to Sham group). n=3 mice per group. *p<0.05, vs Sham, $^{\#}p$<0.05, Vs MI-sus.

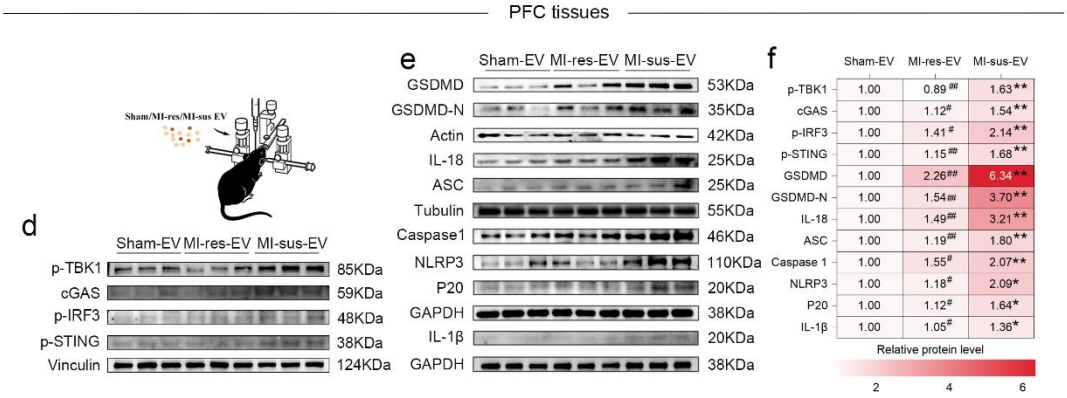
(f–j) Quantitative analysis of sucrose preference (f), total movement distance, (g) central region distance (h), immobility time in TST (i)and immobility time in FST (j) among groups. n=9 mice per group, One-way ANOVA (f, g, j), Kruskal-Wallis test (h), and Brown-Forsythe and Welch ANOVA (i), *p<0.05, **p<0.01, Vs Sham-EV, $^{\#}p$<0.05, $^{\#\#}p$<0.01, Vs MI-sus-EV.

(k) Representative H&E staining of the PFC in Sham-EV, MI-res-EV, and MI-sus-EV groups. Scale bar, 100 μm.

(l) Representative Nissl staining of the PFC in the three groups. Scale bar, 100 μm.

(m–p) Western blot analysis (m) and quantification of synaptic proteins PSD95 (n), GAP43 (o), and SYN (p) in the PFC. n=3 mice per group. One-way ANOVA, **p<0.01, Vs Sham-EV, $^{\#}p$<0.05, $^{\#\#}p$<0.01, Vs MI-sus-EV. Data are expressed as mean ± SD.


PFC tissues
a
Sham
MI-res
MI-sus
p-TBK1
cGAS
p-IRF3
p-STING
Vinculin
85KDa
59KDa
48KDa
38KDa
124KDa
b
Sham
MI-res
MI-sus
NLRP3
Caspase1
P20
GAPDH
ASC
GAPDH
GSDMD
GSDMD-N
IL-18
Actin
IL-1β
Tubulin
110KD
46KDa
20KDa
38KDa
25KDa
38KDa
53KDa
35KDa
25KDa
42KDa
18KDa
55KDa
c
Sham MI-res MI-sus
p-TBK1 1.00 1.02# 1.42*
cGAS 1.00 0.96## 1.87**
p-IRF3 1.00 2.20## 6.59**
p-STING 1.00 1.57# 2.08**
NLRP3 1.00 1.19# 1.52**
Caspase 1 1.00 1.09# 1.46**
P20 1.00 1.10# 1.46*
ASC 1.00 0.97# 1.35*
GSDMD 1.00 1.52# 2.52**
GSDMD-N 1.00 1.44# 2.86*
IL-18 1.00 1.29# 2.67**
IL-1β 1.00 1.12# 1.48**
Relative protein level
2
4
6


PFC tissues
Sham/MI-res/MI-sus EV
d
Sham-EV MI-res-EV MI-sus-EV
p-TBK1
cGAS
p-IRF3
p-STING
Vinculin
85KDa
59KDa
48KDa
38KDa
124KDa
e
Sham-EV MI-res-EV MI-sus-EV
GSDMD
GSDMD-N
Actin
IL-18
ASC
Tubulin
Caspase1
NLRP3
P20
GAPDH
IL-1β
GAPDH
53KDa
35KDa
42KDa
25KDa
25KDa
55KDa
46KDa
110KDa
20KDa
38KDa
20KDa
38KDa
f
Sham-EV MI-res-EV MI-sus-EV
p-TBK1 1.00 0.89## 1.63**
cGAS 1.00 1.12# 1.54**
p-IRF3 1.00 1.41# 2.14**
p-STING 1.00 1.15## 1.68**
GSDMD 1.00 2.26## 6.34**
GSDMD-N 1.00 1.54## 3.70**
IL-18 1.00 1.49## 3.21**
ASC 1.00 1.19## 1.80**
Caspase 1 1.00 1.55# 2.07**
NLRP3 1.00 1.18# 2.09*
P20 1.00 1.12# 1.64*
IL-1β 1.00 1.05# 1.36*
Relative protein level
2
4
6

645
646

Fig 3 Activation of cGAS-STING and pyroptosis in prefrontal cortex after myocardial infarction and intracerebral EV injection

(a) Western blot analysis of cGAS-STING pathway-related proteins (p-TBK1, cGAS, p-IRF3, p-STING) in the PFC of Sham, MI-res, and MI-sus mice.

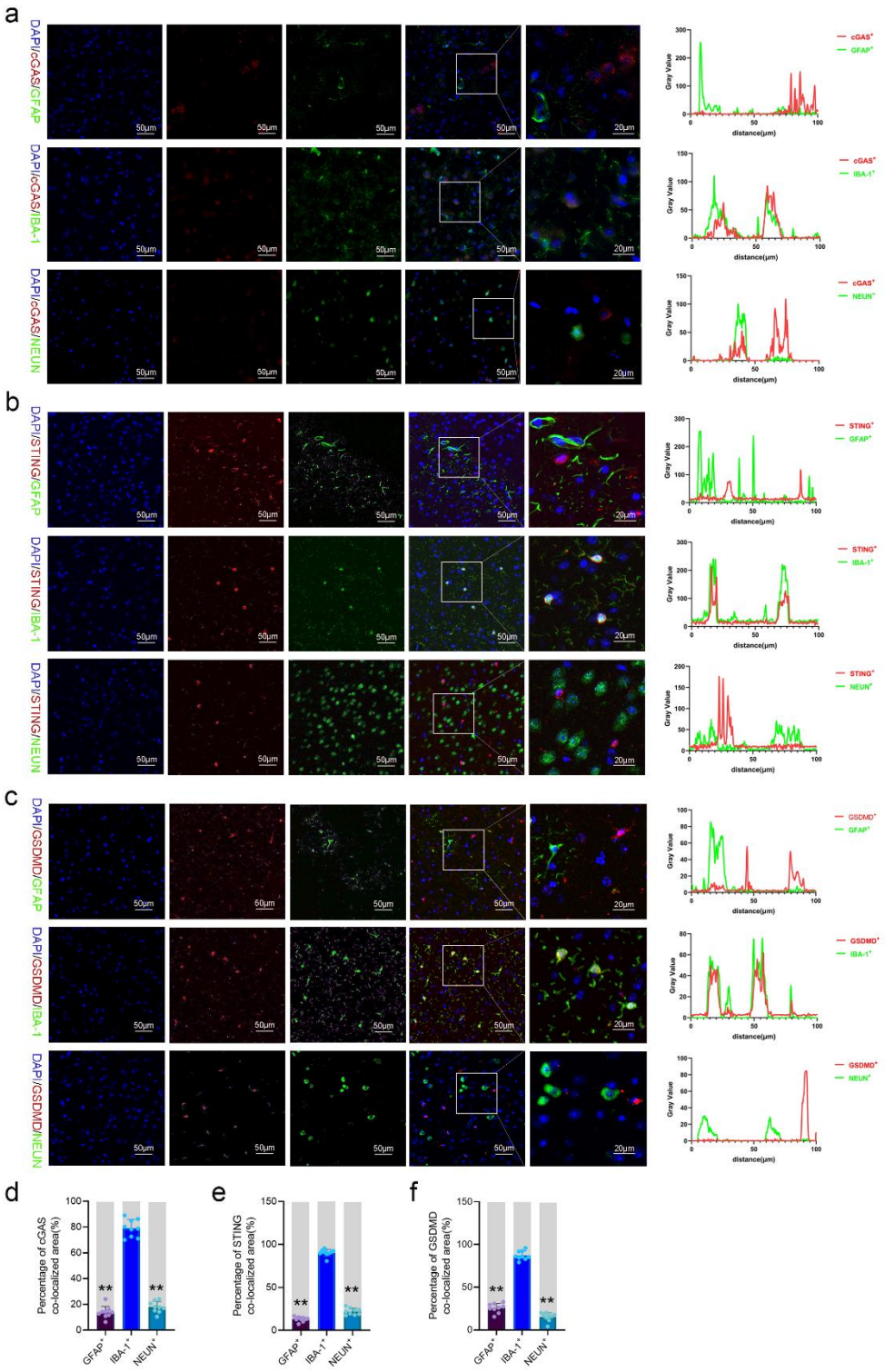
(b) Western blot analysis of pyroptosis-related proteins (NLRP3, Caspase1, P20, ASC, GSDMD, GSDMD-N, IL-18, IL-1β) in the PFC.

(c) Heatmap showing the relative protein levels of cGAS-STING and pyroptosis-related proteins in the PFC, n=3 mice per group. One-way ANOVA, $^{**}p<0.01$ vs. Sham, $^{\#}p<0.05$, $^{\#\#}p<0.01$, vs MI-sus

(d) Western blot analysis of cGAS-STING pathway-related proteins (p-TBK1, cGAS, p-IRF3, p-STING) in the PFC of mice treated with Sham-EV, MI-res-EV, or MI-sus-EV.

(e) Western blot analysis of pyroptosis-related proteins (GSDMD, GSDMD-N, IL-18, ASC, NLRP3, Caspase1, P20, IL-1β) in the PFC of EV-treated mice.

(f) Heatmap showing the relative protein levels of cGAS-STING and pyroptosis-related proteins in the PFC of EV-treated mice, n=3 mice per group. One-way ANOVA, $^{*}p<0.05$, $^{**}p<0.01$, Vs Sham-EV, $^{\#}p<0.05$, $^{\#\#}p<0.01$, Vs MI-sus-EV. Data are expressed as mean ± SD.


a
DAPI/cGAS/GFAP
DAPI/cGAS/IBA-1
DAPI/cGAS/NEUN
b
DAPI/STING/GFAP
DAPI/STING/IBA-1
DAPI/STING/NEUN
c
DAPI/GSDMD/GFAP
DAPI/GSDMD/IBA-1
DAPI/GSDMD/NEUN
50μm
20μm
Gray Value
distance(μm)
cGAS+
GFAP+
IBA-1+
NEUN+
STING+
GSDMD+
d
Percentage of cGAS co-localized area(%)
e
Percentage of STING co-localized area(%)
f
Percentage of GSDMD co-localized area(%)
GFAP+
IBA-1+
NEUN+
**

664
665

Fig 4 cGAS-STING signaling and GSDMD-mediated pyroptosis are predominantly localized in PFC microglia

(a–c) Representative immunofluorescence staining showing the co-localization of cGAS (a), STING (b), and GSDMD (c) with cell-type-specific markers in the PFC. GFAP (green) marks astrocytes, IBA-1 (green) marks microglia, and NEUN (green) marks neurons. Nuclei were counterstained with DAPI (blue). Scale bars, 50 μm and 20 μm. Fluorescence intensity profiles along the indicated lines are shown on the right.

(d–f) Quantification of the percentage of cGAS-, STING-, and GSDMD-co-localized area with $GFAP^+$, $IBA\text{-}1^+$, and $NEUN^+$ cells, respectively. n=3 mice per group, with 10 images analyzed per mouse. One-way ANOVA, $^*p<0.05$, $^{**}p<0.01$, vs Sham, $^{\#}p<0.05$, $^{\#\#}p<0.01$, vs MI-sus, Data are expressed as mean ± SD.

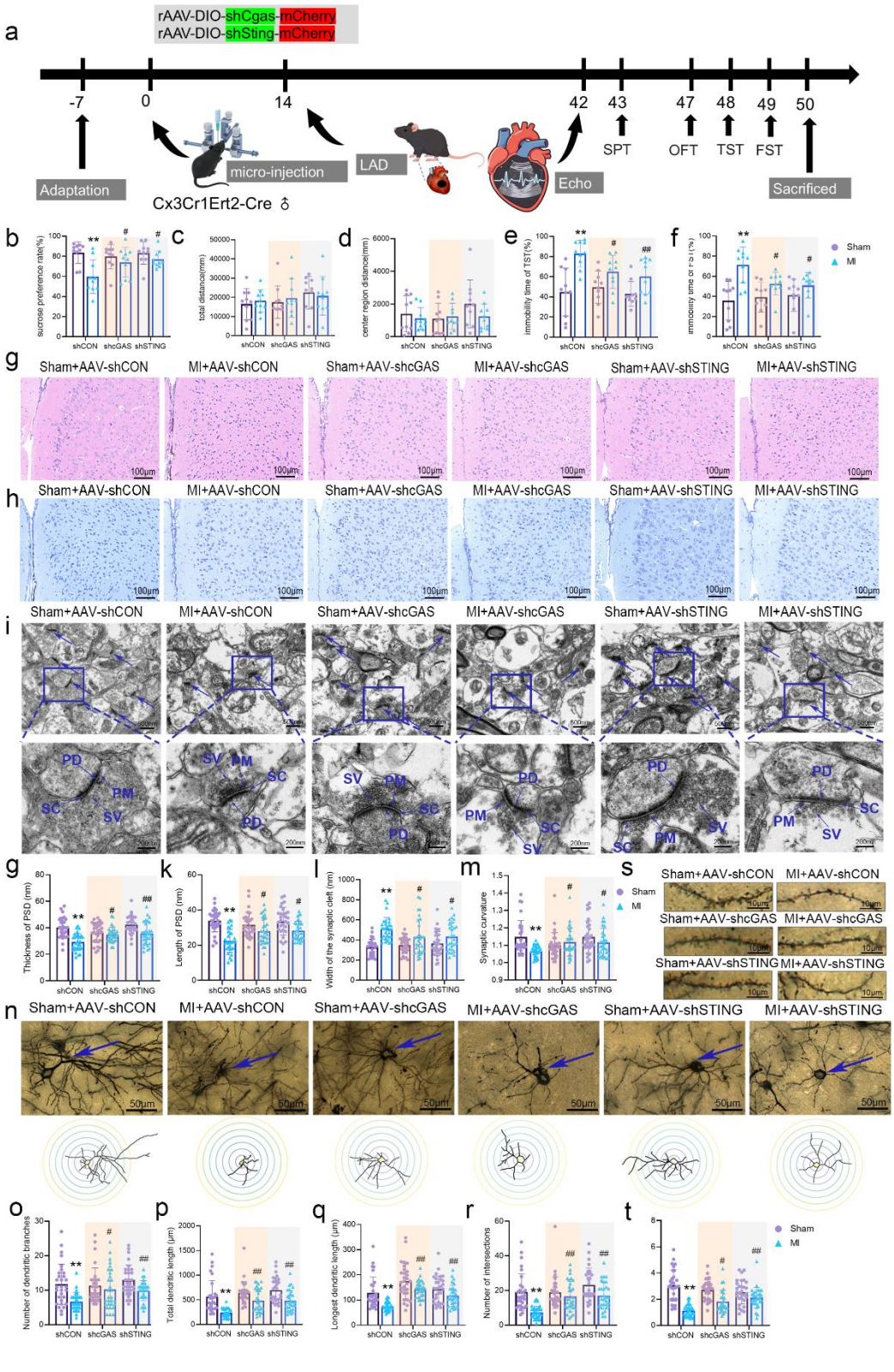

a
rAAV-DIO-shCgas-mCherry
rAAV-DIO-shSting-mCherry
-7
0
14
42
43
47
48
49
50
Adaptation
micro-injection
Cx3Cr1Ert2-Cre ♂
LAD
Echo
SPT
OFT
TST
FST
Sacrificed
b
c
d
e
f
Sham
MI
shCON
shcGAS
shSTING
g
Sham+AAV-shCON
MI+AAV-shCON
Sham+AAV-shcGAS
MI+AAV-shcGAS
Sham+AAV-shSTING
MI+AAV-shSTING
h
i
PD
PM
SC
SV
g
k
l
m
s
n
o
p
q
r
t

Fig 5 cGAS-STING deficiency ameliorates post-MI depression and PFC synaptic injury

(a) Schematic diagram of the experimental timeline for microglia-specific knockdown of cGAS or STING in Cx3Cr1Ert2-Cre mice using rAAV-DIO-shCgas-mCherry or rAAV-DIO-shSting-mCherry.

(b–f) Quantitative analysis of sucrose preference (b), total movement distance (c), central region distance (d), immobility time in TST (e)and immobility time in FST (f) among groups. n=10 mice per group. One-way ANOVA (b, e), Brown-Forsythe and Welch ANOVA (f) and Kruskal-Wallis test (c, d), *p<0.05, **p<0.01, Sham-shCON, $^{\#}p$<0.05, $^{\#\#}p$<0.01, MI+AAV-shCON.

(g) Representative H&E staining of the PFC in the six groups. Scale bar, 100 μm.

(h) Representative Nissl staining of the PFC in the six groups. Scale bar, 100 μm.

(i) Representative TEM micrographs of synapses in the PFC. Presynaptic membrane (PM), postsynaptic density (PD), synaptic cleft (SC), and synaptic vesicles (SV) are labeled. Scale bar, 500 nm and 200 nm.

(j–m) Quantification analysis of PSD thickness (j), PSD length (k), width of the synaptic cleft (l), and synaptic curvature (m) in the PFC. n=3 mice per group, with 10 synapses analyzed per mouse. One-way ANOVA (j, k) and Kruskal-Wallis test (l, m), **p<0.01, Sham-shCON, $^{\#}p$<0.05, $^{\#\#}p$<0.01, MI+AAV-shCON.

(n) Representative Golgi staining of pyramidal neurons in the PFC and corresponding Sholl analysis diagrams showing dendritic complexity. Arrows point to representative pyramidal neurons, scale bar, 50 μm.

(o–r) Quantification of the number of dendritic branches (o), total dendritic length (p), longest dendritic length (q) and number of intersections (r) by Sholl analysis, Kruskal-Wallis test, *p<0.05, **p<0.01, vs Sham+AAV-shCON, $^{\#\#}p$<0.01, vs MI+AAV-shCON.

(s) Representative images of dendritic spines in the PFC. Scale bar, 10 μm.

(t) Quantification of spine density in the three groups, n=3 mice per group, with 10 dendritic segments analyzed per mouse. Kruskal-Wallis test, *p<0.05, **p<0.01, vs Sham+AAV-shCON, $^{\#\#}p$<0.01, vs MI+AAV-shCON. Data are expressed as mean ± SD.

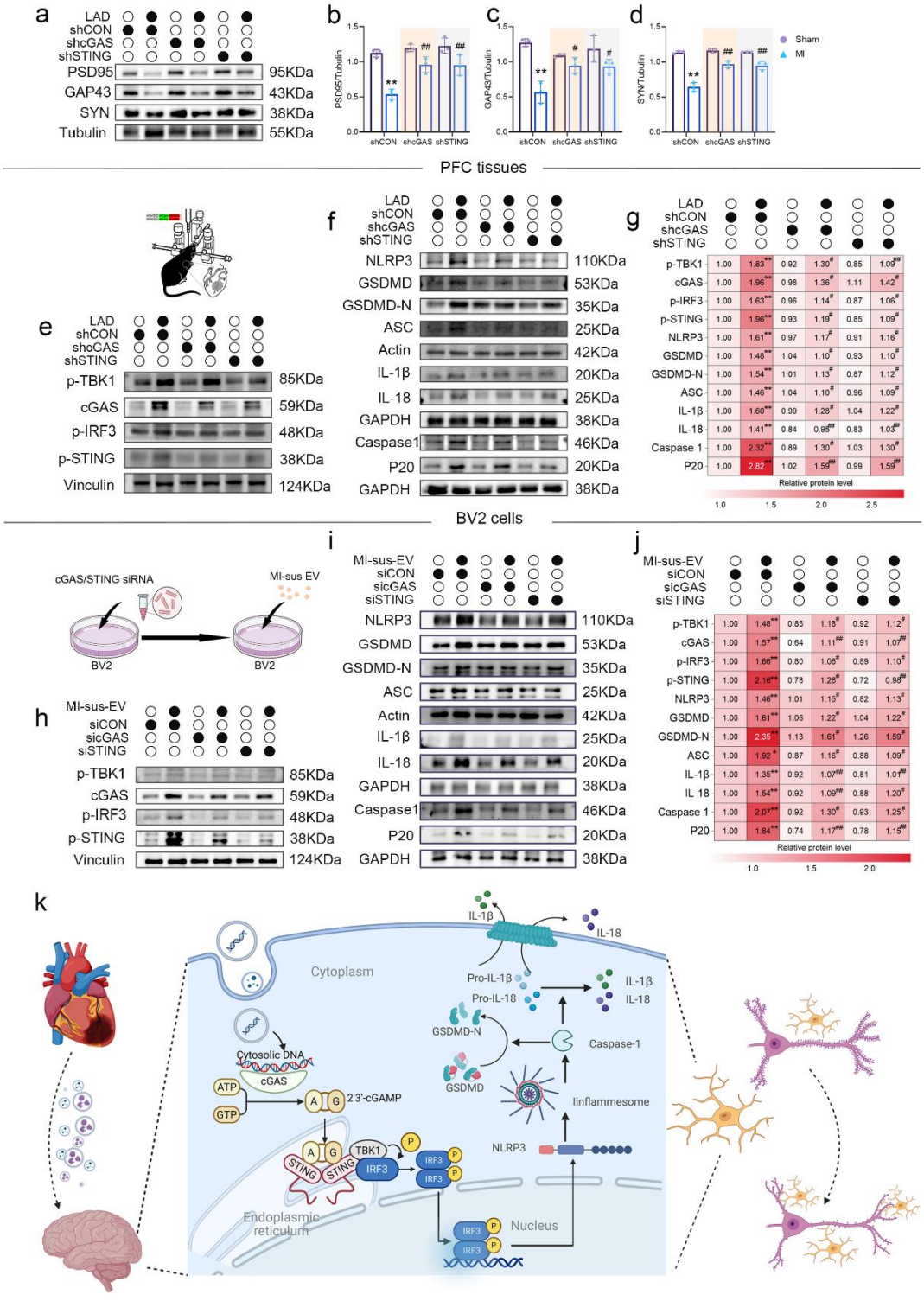

a
LAD
shCON
shcGAS
shSTING
PSD95
GAP43
SYN
Tubulin
95KDa
43KDa
38KDa
55KDa
b
PSD95/Tubulin
c
GAP43/Tubulin
d
SYN/Tubulin
shCON
shcGAS
shSTING
Sham
MI
PFC tissues
e
p-TBK1
cGAS
p-IRF3
p-STING
Vinculin
85KDa
59KDa
48KDa
38KDa
124KDa
f
NLRP3
GSDMD
GSDMD-N
ASC
Actin
IL-1β
IL-18
GAPDH
Caspase1
P20
110KDa
53KDa
35KDa
25KDa
42KDa
20KDa
46KDa
g
Relative protein level
BV2 cells
cGAS/STING siRNA
MI-sus EV
BV2
h
MI-sus-EV
siCON
sicGAS
siSTING
i
j
k
Cytoplasm
Cytosolic DNA
cGAS
ATP
GTP
2'3'-cGAMP
TBK1
IRF3
STING
Pro-IL-1β
Pro-IL-18
GSDMD-N
GSDMD
Caspase-1
linflammesome
NLRP3
Endoplasmic reticulum
Nucleus

Fig 6 cGAS-STING blockade suppresses microglial cGAS-STING activation and pyroptosis both in vivo and in vitro

(a) Western blot analysis of synaptic proteins (PSD95, GAP43, SYN) in the PFC of mice.

(b–d) Quantification of PSD95, GAP43, and SYN protein levels, n=3 mice per group. One-way ANOVA, $^{**}p<0.01$, vs Sham+AAV-shCON, $^{\#}p<0.05$, $^{\#\#}p<0.01$, vs MI+AAV-shCON.

(e) Western blot analysis of cGAS-STING pathway-related proteins (p-TBK1, cGAS, p-IRF3, p-STING) in the PFC.

(f) Western blot analysis of pyroptosis-related proteins (NLRP3, GSDMD, GSDMD-N, ASC, IL-1β, IL-18, Caspase1, P20) in the PFC.

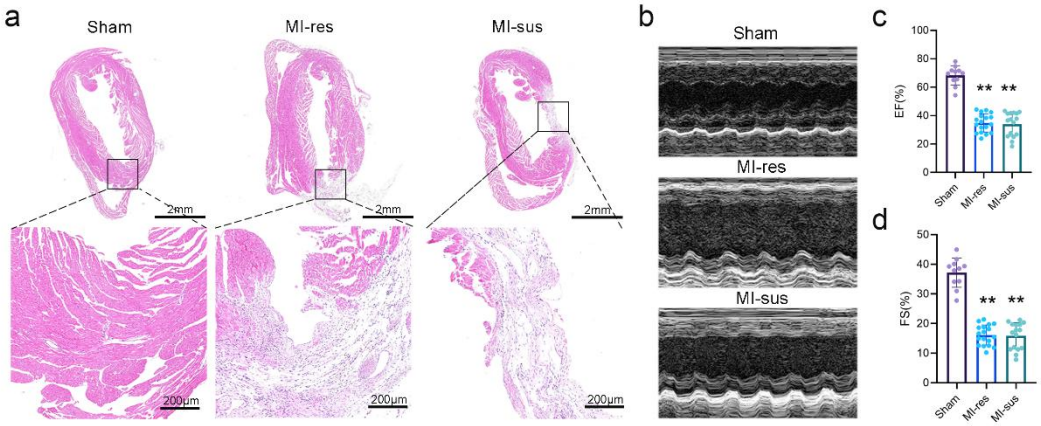
(g) Heatmap showing the relative protein levels of cGAS-STING and pyroptosis-related proteins levels, n=3 mice per group. One-way ANOVA, $^{**}p<0.01$, vs Sham+AAV-shCON, $^{\#}p<0.05$, $^{\#\#}p<0.01$, vs MI+AAV-shCON.

(h) Western blot analysis of cGAS-STING pathway proteins (p-TBK1, cGAS, p-IRF3, p-STING) in BV2 cells.

(i) Western blot analysis of pyroptosis-related proteins (NLRP3, GSDMD, GSDMD-N, ASC, IL-1β, IL-18, Caspase1, P20) in BV2 cells.

(j) Heatmap showing the relative protein levels of cGAS-STING and pyroptosis-related proteins in BV2 cells. n=3 independent experiments per group. $^{**}p<0.01$, vs Sham-EV+ sICON, $^{\#}p<0.05$, $^{\#\#}p<0.01$, vs MI-sus-EV+siCON. Data are expressed as mean ± SD.

(k) Schematic diagram of the proposed mechanism.


a
Sham
MI-res
MI-sus
2mm
200μm
b
Sham
MI-res
MI-sus
c
EF(%)
d
FS(%)
**
Sham
MI-res
MI-sus

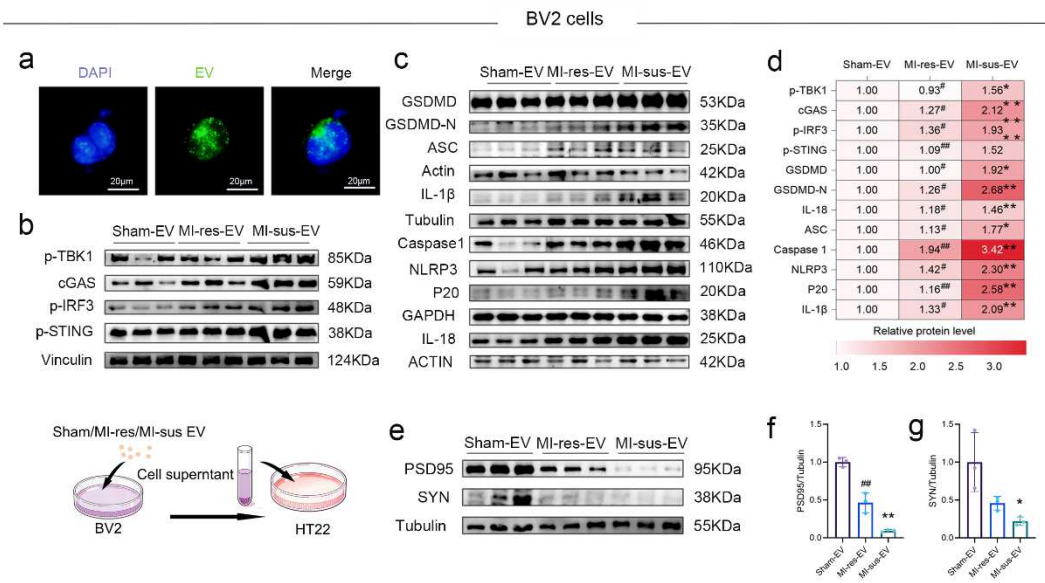
735
736

Fig S1 Cardiac histology and function assessment in post-myocardial infarction mice.

(a) Representative H&E staining of heart sections from Sham, MI-res, and MI-sus mice. Scale bar, 2 mm and 200 μm.

(b) Representative M-mode echocardiography images of the left ventricle in the three groups.

(c–d) Quantification of ejection fraction (EF) (c) and fractional shortening (FS) (d) in the three groups. n = 11 (Sham), 18 (MI-res), 16 (MI-sus)m One-way ANOVA, *$p<0.05$, **$p<0.01$, vs Sham. Data are expressed as mean ± SD.


BV2 cells
a
DAPI
EV
Merge
20μm
b
Sham-EV MI-res-EV MI-sus-EV
p-TBK1 85KDa
cGAS 59KDa
p-IRF3 48KDa
p-STING 38KDa
Vinculin 124KDa
c
Sham-EV MI-res-EV MI-sus-EV
GSDMD 53KDa
GSDMD-N 35KDa
ASC 25KDa
Actin 42KDa
IL-1β 20KDa
Tubulin 55KDa
Caspase1 46KDa
NLRP3 110KDa
P20 20KDa
GAPDH 38KDa
IL-18 25KDa
ACTIN 42KDa
d
Sham-EV MI-res-EV MI-sus-EV
p-TBK1 1.00 0.93# 1.56*
cGAS 1.00 1.27# 2.12**
p-IRF3 1.00 1.36# 1.93**
p-STING 1.00 1.09## 1.52
GSDMD 1.00 1.00# 1.92*
GSDMD-N 1.00 1.26# 2.68**
IL-18 1.00 1.18# 1.46**
ASC 1.00 1.13# 1.77*
Caspase 1 1.00 1.94## 3.42**
NLRP3 1.00 1.42# 2.30**
P20 1.00 1.16## 2.58**
IL-1β 1.00 1.33# 2.09**
Relative protein level
1.0 1.5 2.0 2.5 3.0
Sham/MI-res/MI-sus EV
Cell superntant
BV2
HT22
e
Sham-EV MI-res-EV MI-sus-EV
PSD95 95KDa
SYN 38KDa
Tubulin 55KDa
f
PSD95/Tubulin
Sham-EV
MI-res-EV
MI-sus-EV
g
SYN/Tubulin
Sham-EV
MI-res-EV
MI-sus-EV

747
748

Fig S2 EV-induced cGAS-STING activation and pyroptosis in BV2 cells impairs neuronal synaptic integrity

(a) Representative immunofluorescence images showing the internalization of EVs (green) by BV2 cells, with nuclei counterstained by DAPI (blue). Scale bar, 20 μm.

(b) Western blot analysis of cGAS-STING pathway-related proteins (p-TBK1, cGAS, p-IRF3, p-STING) in BV2 cells treated with Sham-EV, MI-res-EV, or MI-sus-EV.

(c) Western blot analysis of pyroptosis-related proteins (GSDMD, GSDMD-N, ASC, IL-1β, Caspase1, NLRP3, P20, IL-18) in EV-treated BV2 cells.

(d) Heatmap showing the relative protein levels of cGAS-STING and pyroptosis-related proteins in EV-treated BV2 cells, n=3 independent experiments per group. One-way ANOVA, *p<0.05, **p<0.01, Vs Sham-EV, #p<0.05, ##p<0.01, Vs MI-sus-EV

(e) Western blot analysis of synaptic proteins (PSD95, SYN) in HT22 neurons treated with the supernatant of EV-stimulated BV2 cells.

(f–g) Quantification of PSD95 and SYN protein levels, n=3 independent experiments per group. One-way ANOVA, *p<0.05, **p<0.01 vs. Sham-EV, ##p<0.01, Vs MI-sus-EV.

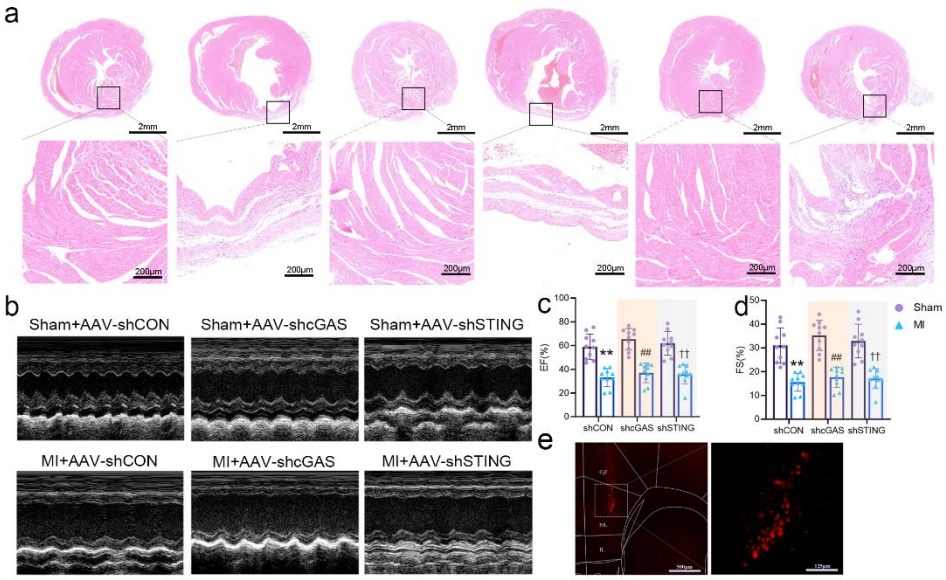

a
2mm
200μm
b
Sham+AAV-shCON
Sham+AAV-shcGAS
Sham+AAV-shSTING
MI+AAV-shCON
MI+AAV-shcGAS
MI+AAV-shSTING
c
EF(%)
**
##
††
shCON
shcGAS
shSTING
d
FS(%)
Sham
MI
e

Fig S3 cGAS-STING signaling and GSDMD-mediated pyroptosis are predominantly localized in PFC microglia

(a) Representative H&E staining of heart sections from Sham+AAV-shCON, Sham+AAV-shcGAS, Sham+AAV-shSTING, MI+AAV-shCON, MI+AAV-shcGAS, and MI+AAV-shSTING mice. Scale bars: 2 mm and 200.

(b) Representative M-mode echocardiography images of the left ventricle in each group.

(c–d) Quantification of EF (c) and FS (d). n=10 mice per group. One-way ANOVA, $^{**}p<0.01$ vs. Sham+AAV-shCON; $^{\#\#}p<0.01$ vs. Sham+AAV-shcGAS, $^{\#\#}p<0.01$ vs. Sham+AAV-shcGAS, ††$p<0.01$ vs. Sham+AAV-shSTING.

(e) Representative fluorescence images showing microglial-specific AAV-mCherry expression in the mouse brain. Scale bar: 500 μm and 125 μm. Data are expressed as mean ± SD.